Photothermal Microscopy of the Core of Dextran-Coated Iron Oxide Nanoparticles During Cell Uptake

Lara K. Bogart,[†,*] Arthur Taylor,[‡] Yann Cesbron,[†] Patricia Murray,[‡] and Raphaël Lévy[†]

[†]Structural and Chemical Biology, Institute of Integrative Biology, and [‡]Institute of Translational Medicine, University of Liverpool, United Kingdom

ABSTRACT

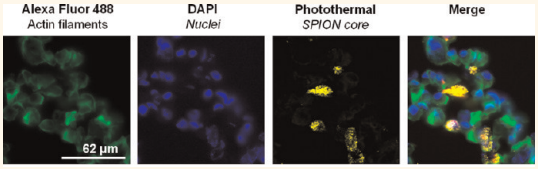

A detailed understanding of cellular interactions with superparamagnetic iron oxide nanoparticles (SPIONs) is critical when their biomedical applications are considered. We demonstrate how photothermal microscopy can be used to follow the cellular uptake of SPIONs by direct imaging of the iron oxide core. This offers two important advantages when compared with current strategies employed to image magnetic cores: first, it is nondestructive and is therefore suitable for studies of live cells and, second, it offers a higher sensitivity and resolution, thus allowing for the identification of low levels of SPIONs within a precise subcellular location. We have shown that this technique may be applied to the imaging of both cell monolayers and cryosections. In the former we have demonstrated the role of temperature on the rate of endocytosis, while in the latter we have been able to identify cells labeled with SPIONs from a mixed population containing predominantly unlabeled cells. Direct imaging of the SPION core is of particular relevance for research involving clinically approved SPIONs, which do not contain fluorescent tags and therefore cannot be detected *via* fluorescence microscopy.

KEYWORDS: superparamagnetic iron oxide nanoparticles · photothermal imaging · cellular uptake of nanoparticles · membrane binding of nanoparticles · cryosections

Magnetic nanoparticles have seen a rapid growth in biomedicine and are currently used for magnetic sensing, targeted drug delivery, hyperthermia treatment, and magnetic resonance imaging (MRI).[1,2] The combination of chemical stability, low toxicity, and biodegradability of iron oxide-based nanoparticles means they have become an increasingly common choice material in such applications.[3,4] As the dimensions of iron oxide nanoparticles are reduced to the order of tens of nanometers the magnetic behavior becomes superparamagnetic: in the absence of an applied field the net magnetization of the ensemble is zero which facilitates colloidal stability (provided that the particles are small), while the application of a large magnetic field yields a large magnetization that can be harnessed for actuation and imaging.[5] Although initially developed as MRI contrast agents for the liver and spleen, functionalized core–shell superparamagnetic iron oxide nanoparticles (SPIONs) have recently been proposed as a solution for tracking cells *in vivo,* a strategy that requires cell labeling with SPIONs prior to their administration.[6,7]

The use of SPIONs for cell tracking applications has important implications in terms of materials design, particularly as the consequences of cellular internalization on the integrity of the nanoparticle are by no means fully understood.[8,9] Indeed, it is well reported that both the iron oxide core and its surface coating can degrade with time.[10,11] Small changes in the chemical composition of the core (which can be either Fe_3O_4 or γ-Fe_2O_3, or a nonstoichiometric combination of the two), the degree of crystallinity, and the diameter can result in large changes in the magnetic behavior.[12] A thorough knowledge of the effects of intracellular localization and microenvironment on the structure and, consequently, the magnetic properties of SPIONs is imperative for the rational design of cell tracking probes.

Progress in understanding the cellular fate of SPIONs in biological processes is limited by the lack of techniques suitable for both imaging and magnetic characterization in live cells. Current studies aimed at elucidating the localization and fate of SPIONs in cells and tissues mostly rely on a combination of transmission electron microscopy (TEM) and Prussian blue staining.[13] While TEM offers unrivalled resolution, both Prussian blue and TEM are limited to the study of fixed cells and tissues, which

* Address correspondence to lara.bogart@liverpool.ac.uk, rapha@liverpool.ac.uk.

Received for review February 27, 2012 and accepted June 2, 2012.

Published online June 02, 2012
10.1021/nn300868z

restricts the study of localization of SPIONs to fixed time points. A dynamic evaluation of the uptake can be achieved using live cell imaging, but SPIONs are not intrinsically fluorescent and lack optical contrast to be detected by classical optical microscopy methods. Optical microscopy imaging has been performed by encapsulating SPIONs within a metal shell to yield multimodal contrast probes that can be targeted and detected using photothermal microscopy;[14,15] although, a potential limitation of this approach is that the addition of such a shell may affect the magnetic properties of the core.[16] Live cell imaging of SPIONS can be achieved by the incorporation of a fluorophore into the ligand shell;[11] however, it has been shown that SPIONs are exposed to a continuous decrease in pH during endocytosis, which can result in rapid degradation and might then lead to a physical separation of the shell and the core.[17,18] In addition, enzymatic cleavage may also lead to the deterioration of the shell and to the subsequent physical separation of both the shell and the core.[19] As a consequence, the use of fluorophores conjugated to the shell of the nanoparticle might not be a reliable method for identifying the location of the core. Understanding of the long-term fate requires use of new microscopy techniques that offer the simultaneous and independent imaging of both the core and the shell of SPIONs in live cells.

Here we demonstrate that photothermal microscopy can be used for the direct imaging of the SPION core in both fixed cells and cryosections, as well as in live cell monolayers. Photothermal imaging is an optical technique in which energy from a time-modulated laser beam (heating beam) is absorbed by the nanoparticle cores present in the focal volume and converted to thermal energy. The local change of temperature around a core induces a spatially modulated refractive index profile in its vicinity, within which a second nonresonant probe laser beam is scattered to produce a distinctive frequency-shifted scattered field. The resolution of the technique is determined by the laser beam profiles, while the signal is proportional to both the heating beam intensity and to the absorption cross-section of the nanoparticle.[20] This technique is currently established for the detection of metal nanoparticles such as gold[21,22] and silver,[20] as well as quantum dots[23] and single-walled carbon nanotubes.[24,25]

In this work, correlative microscopy of the shell (fluorescence) and of the iron oxide core (photothermal) in cells has been performed and is compared to both TEM imaging and Prussian blue staining. Quantitative analysis of the photothermal signal *via* a single-cell analysis is in excellent agreement with inductively coupled plasma optical emission spectroscopy (ICP–OES) measurements. Both the sensitivity and the resolution of photothermal imaging compare favorably with Prussian blue staining. Initial toxicity experiments indicate that photothermal imaging is compatible with live cell imaging, with live cell results indicating a slow entry of the materials into a kidney-derived stem cell line after an initial build-up at the membrane. Photothermal imaging on both live and fixed cells incubated for 5 h at 4 °C indicate that the membrane binding is reversible and that cellular uptake is strongly temperature dependent. Finally, we have applied this technique to study cryosections of cell pellets and can distinguish cells labeled with SPIONs from unlabeled cells. The results presented here suggest that photothermal microscopy will allow for the systematic investigation of both the intracellular localization and cell retention properties of SPIONs.

RESULTS AND DISCUSSION

As the photothermal technique is based upon the absorption of the heating beam by the nanoparticle—with the measured photothermal signal being directly proportional to the absorption cross-section of the nanoparticle—it is necessary to begin by establishing the absorbance properties of SPIONs. Supporting Information, Figure S1a presents a UV–vis extinction spectrum of SPIONs in water, in which the wavelengths of both the heating and probe lasers used in photothermal imaging are also indicated. A steady extinction decrease can be seen, with two small peaks present at 480 and 560 nm, respectively. It is suggested that the peak at 480 nm is due to the absorbance of the iron oxide, with Kim *et al.*[26] reporting a comparable extinction spectrum for Endorem SPIONs with a small peak at similar wavelengths. The peak at 560 nm corresponds to the excitation band of the Rhodamine B fluorophore.[27]

There is little reported in the literature for the absorbance properties of SPIONs; however, an understanding of the origin of this peak can be gained by reviewing the literature of other iron oxide-based devices. Iron oxide thin films and nanoparticles are used in a wide range of technological applications, including magnetic recording devices,[28] solar cells,[29] and semiconductor devices,[30] the latter of which are based wholly on the absorbance behavior of the iron oxides. Indeed, it is well reported that the iron oxides absorb across the entire visible range;[31,32] the combination of a strong absorbance of iron oxide in the visible region with a well-defined band gap (2.2 eV) has seen the rise of both forms of Fe_2O_3 (α-Fe_2O_3 and γ-Fe_2O_3) thin films in both photocatalyst and photoanode devices.[29,33,34] It is these absorbance properties that form the physical basis of this investigation.

As a first proof of principle, we have imaged fluorescently labeled SPIONS adsorbed on a surface *via* fluorescence and photothermal microscopy using the setup shown in Supporting Information, Figure S2. The sample was prepared by depositing a droplet containing positively charged SPIONs to a negatively charged polymer-coated glass coverslip. Figure 1 shows the edge of the area that was exposed on SPIONs. Both the

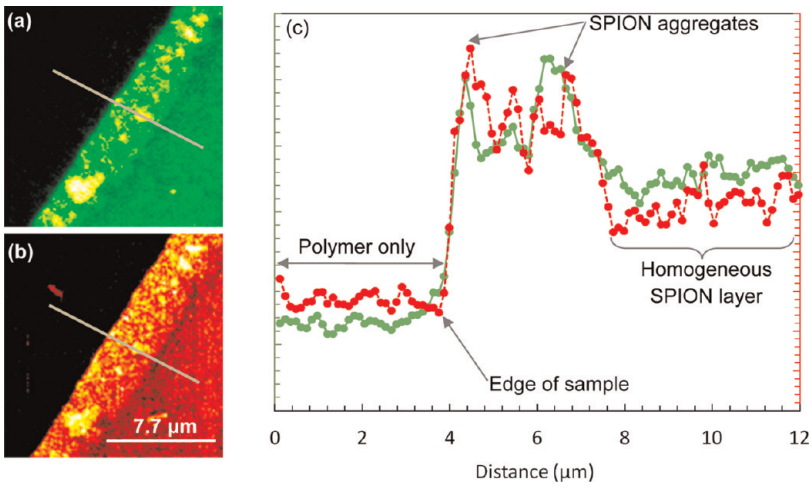

Figure 1. Comparison of (a) fluorescence and (b) photothermal images of SPIONs immobilized on a carboxymethyl dextran surface and (c) line profile of fluorescence (green) and photothermal (red) signal across the line indicated in the images.

fluorescence signal (Figure 1a) and photothermal signal (Figure 1b) can be clearly distinguished from that of the background (left side, dark region). SPION aggregates are evident as "hotspots" along the edge of the drop. A larger image of the droplet edge before and after photothermal scans is presented in Supporting Information, Figure S3; photobleaching of the fluorescence signal after photothermal scanning is clearly visible in Figure S3b, and is due to the proximity of peak excitation wavelength of the fluorophore to the heating laser (555 and 523 nm, respectively).

Quantification of the fluorescence and photothermal signal can be performed by taking line profiles across the same area (Figure 1c). Each line profile shows an initial sharp increase in signal over that of the background in each channel at the edge of the drop, and in particular in the area where there are large SPION aggregates. On the basis of this experiment, we estimate that, under those imaging conditions, the limit of detection is equal to or lower than[35] 530 SPIONs within the focal area. Details of the calculations are provided in the Supporting Information (iii).

To establish the suitability of the technique for imaging biological samples, we have imaged fixed cells that were labeled with SPIONs for 24 h. Figure 2 presents bright field (A–D), fluorescence (E–H), and photothermal imaging (I–L) of (i) cells only and cells incubated with (ii) 1, (iii) 5, and (iv) 25 μg/mL of SPIONs in the cell medium for 24 h. To prevent photobleaching of the fluorophore by the lasers, the fluorescence imaging was performed before the photothermal imaging for each area of interest. A clear increase in both the fluorescence and photothermal signal is observed as the concentration of SPIONs increases, with a small cell-to-cell variation within each field.

There is a strong level of colocalization between the fluorescence and the photothermal signals, with a clear difference between them: in the fluorescence images there is a diffuse signal that increases as SPION concentration increases that is not visible within the corresponding photothermal images. This may be due to partial degradation of the shell, or to out of focus blurring of the wide-field fluorescence image. In addition, there is no signal (either fluorescent or photothermal) from the areas between cells implying that both signals are due to SPIONs taken up by the cells rather than adsorbed to the dish. The localization indicates that the SPIONs are accumulated in perinuclear vesicles, which is further confirmed by TEM images (Supporting Information, Figure S4) showing large numbers of SPIONs enclosed in vesicles.

Quantification of the average photothermal signal per condition has been obtained by performing a single cell analysis (details of which are provided in the Supporting Information (v) with an example of the cell outlines used provided in Figure S5) and has been independently verified using inductively coupled plasma optical emission spectroscopy (ICP–OES) measurements. Values of the mean photothermal signal are compared to the mean iron content per cell for each condition in Table 1.

Figure 3a compares normalized mean values obtained by each technique. An excellent agreement is observed with similar increases in the amount of respective signal between successive concentrations. There is an increase of ~2.5-fold between 1 and 5 μg/mL, while this changes to ~2-fold between 5 and 25 μg/mL. The uptake of SPIONs is not expected to increase linearly with concentration, since the cells eventually begin to saturate with nanoparticles. The minimum amount of SPIONs that can be detected per cell by a statistical analysis of at least 50 single cell photothermal signals can be estimated using Figure 3b. The results suggest that the limit of detection is ~0.2 pg above the physiological amount present within cells.

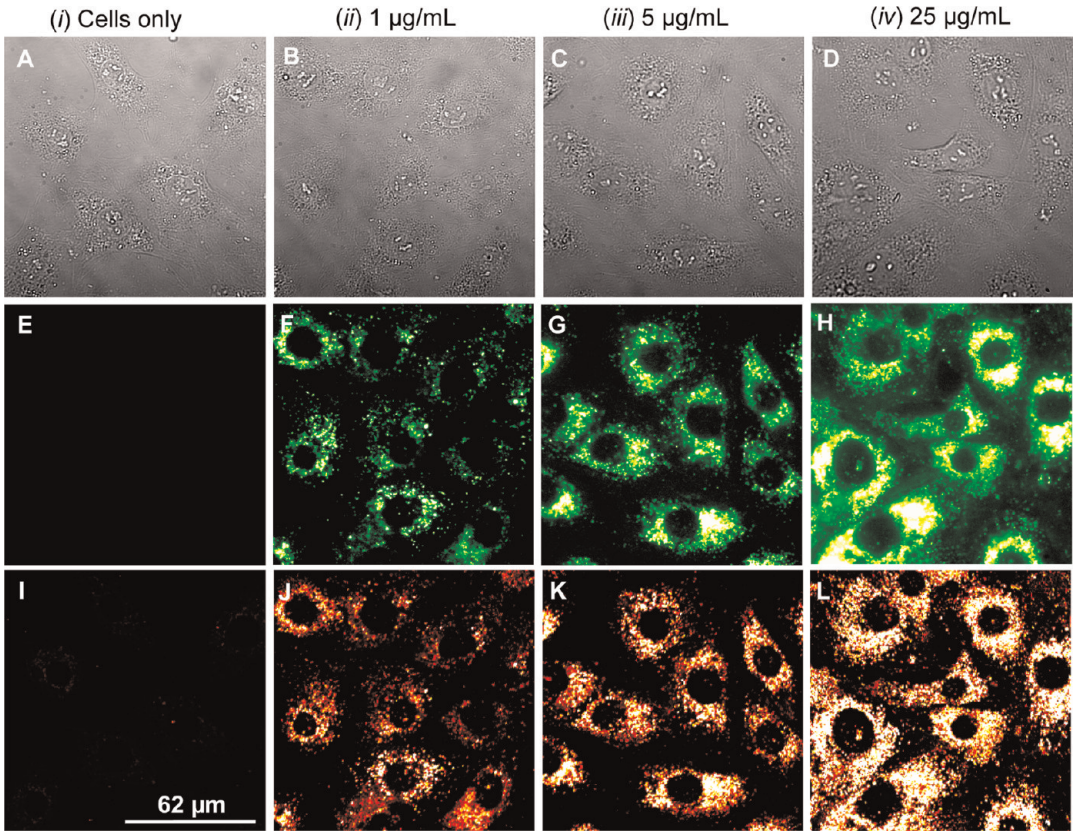

Figure 2. Comparison of bright field imaging (A–D), fluorescence (E–H), and photothermal microscopy (I–L) for (i) cells only and for cells labeled with (ii) 1, (iii) 5, and (iv) 25 μg/mL of SPIONs for 24 h. All fluorescence and photothermal images are presented in false colors using the same brightness and contrast conditions, respectively.

TABLE 1. Comparison of Mean Photothermal Signal Obtained Using Single Cell Analysis to the Mean Amount of Iron Per Cell, as Measured Using ICP–OES

	mean photothermal signal (mV)		mean amount of iron per cell (pg)	
condition	mean	standard deviation	mean	standard deviation
cells only	4.92	1.93	0.52	0.53
1 μg/mL	61.00	26.89	3.10	1.07
5 μg/mL	168.00	18.54	7.05	1.59
25 μg/mL	346.88	77.82	11.22	1.28

Having demonstrated the ability of this technique to directly image the iron oxide core, we have sought to compare the photothermal images to those obtained from standard staining methods often applied to detect iron-based magnetic nanoparticles in cells. Prussian blue staining is a common technique for histological staining of iron, where the intensity of staining is proportional to the amount of iron(III) present within the cell.

Figure 4 presents bright field (A–D), high resolution photothermal (E–H) and Prussian blue staining (I–L) images of (i) unlabeled cells, and of cells labeled with (ii) 1, (iii) 5, and (iv) 25 μg/mL of SPIONs for 24 h. Both the photothermal signal and Prussian blue staining increase as the SPION concentration increases, with each technique appearing sensitive to both high and low levels of intracellular iron. Qualitatively, it can be seen that the signal distribution as measured by photothermal imaging is in excellent agreement with that of the Prussian blue stain, with the hotspots in all cells well matched by each imaging technique.

Quantitative comparisons between the two techniques can be performed by evaluating the variation in signal intensity across sections of the cell, as presented in panels M–P. While the photothermal signal was measured using a photodiode and saved as a greyscale image, the Prussian blue images were captured using a color CCD camera and the images were saved in color (RGB) format. It was therefore necessary to process the images so that only the blue component could be extracted and analyzed. Details of the image analysis performed are provided in the Supporting Information (section (vi)), Figures S6 and S7. Each line profile presents the variation in photothermal signal (red) and Prussian blue signal (blue) in the section indicated by the line in panels E-L. Such profiles reveal that both the sensitivity and resolution provided by photothermal imaging are much greater than that obtained by Prussian blue staining. Indeed, the signal given by Prussian blue is very similar for all three SPION concentrations, which is not the case for the corresponding photothermal signal maxima.

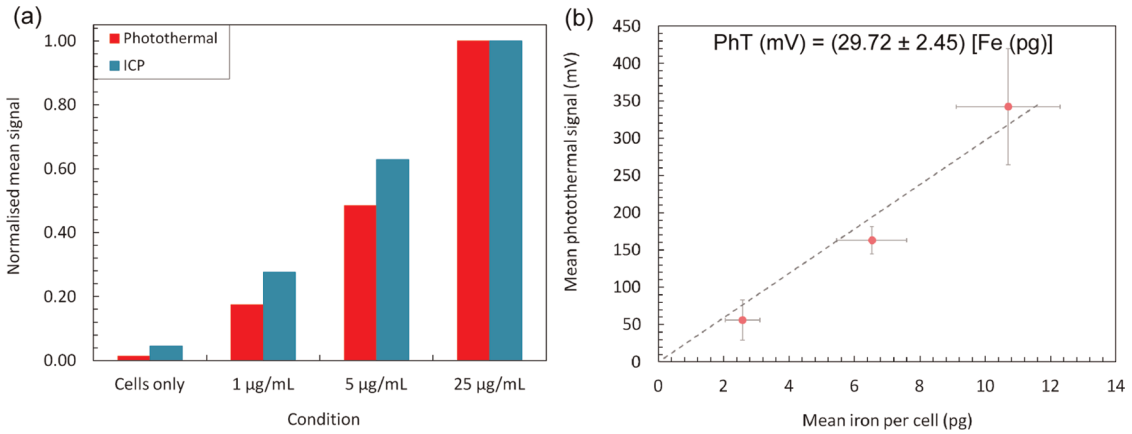

Figure 3. (a) Quantitative comparison of the mean photothermal signal (obtained using single cell analysis (red)) and mean amount of iron per cell (measured by ICP−OES measurements (blue)). Single cell analysis was performed for at least 50 cells per condition; details of which are given in the Supporting Information (v). (b) Mean photothermal signal as a function of iron load per cell, with the corresponding line of best fit to the data.

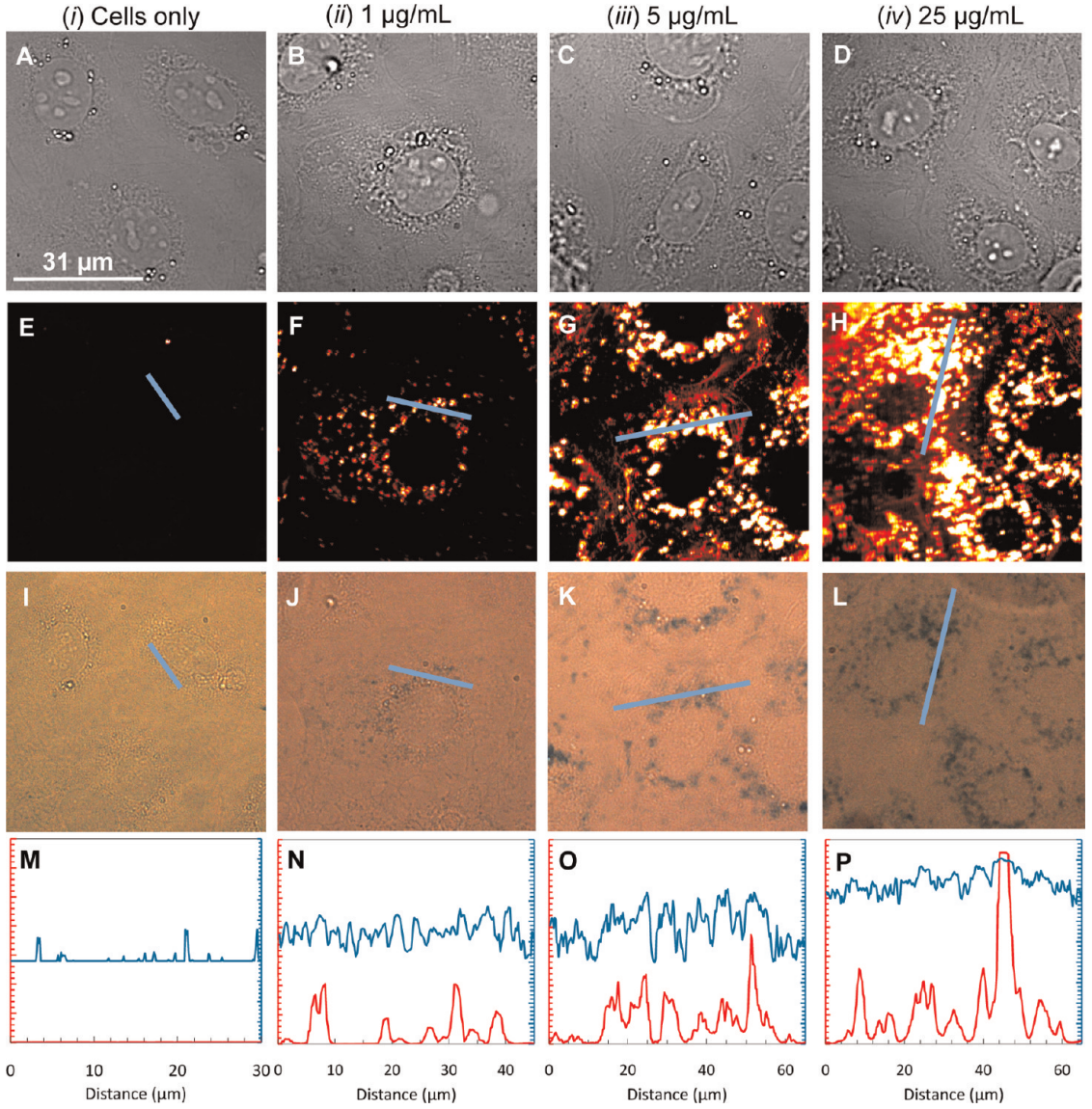

Figure 4. Comparison of bright field imaging (A−D), photothermal microscopy (E−H), and Prussian blue staining (I−L) of (i) cells only and cells labeled with (ii) 1, (iii) 5, and (iv) 25 μg/mL of SPIONs for 24 h. The profiles presented in panels M-P correspond to the variation in photothermal (red) and Prussian blue (blue) signal in the area indicated by the line in each image.

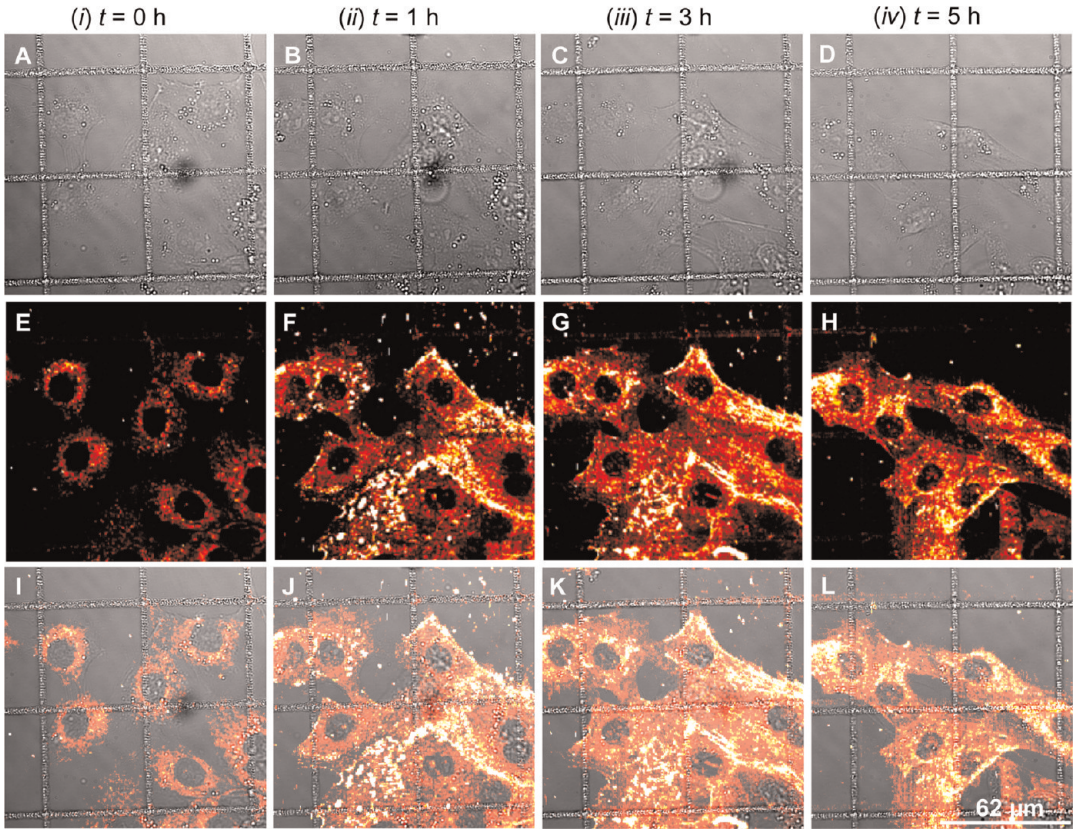

Figure 5. Comparison of bright field (A–D), corresponding photothermal image (E–H) and overlay (I–L) of live cells, with time measured after the addition of SPIONs to the cell medium. All photothermal images are set to same brightness and contrast settings.

In the final section of this study, we demonstrate how photothermal microscopy can be applied to biological studies involving SPIONs. We focus on two examples: real time imaging of the interaction of SPIONs with live cells and the identification of SPION-labeled cells within cryosections of cell pellets. Success in the former will provide time-resolved information on single cells that cannot be obtained with either TEM or Prussian blue staining, while the latter will allow for the identification of labeled cells within tissue sections obtained from explanted organs, thus allowing the identification of migration sites. This is of particular relevance for cell tracking investigations. In addition, the greater sensitivity that is obtained *via* photothermal imaging when compared to Prussian blue staining is of particular significance for long-term investigations on the migration of labeled cells, as cell proliferation in the host results in progressively lower amounts of nanoparticles per cell.[6]

Figure 5 presents representative bright field images (A–D), corresponding photothermal images (E–H), and overlays (I–L) over time for live cells imaged over a 5 h period. The bright field images shown correspond to those taken immediately after photothermal imaging. Bright field images were taken immediately before and after the photothermal images to look for any changes in morphology typically associated with cell death, an example of which can be seen in Supporting Information, Figure S8.

The maximum scale presented here is 20% that used for the images presented in Figure 2, and so allows for the background signal from absorbing species present in the cells to be measured (such as mitochondria[36]). Initially, a photothermal image of unlabeled cells (no SPIONs; t = 0 h) was acquired (Figure 5 (i)) after which the medium was removed and fresh medium containing 5 μg/mL of SPIONs was added directly to the dish.

After waiting for the SPIONs to settle, the same field was imaged using photothermal microscopy every 1 h for a 5 h period, after which the medium was replaced with fresh medium containing both 5 μg/mL of SPIONs and Sytox Orange. This procedure was performed over six different fields with at least five cells per field. The photothermal images presented in panels E and F show a clear difference in the signal once the SPIONs are added to the medium and suggest an accumulation of SPIONs on the cell membrane. This is likely to be the result of the large positive zeta potential (+31 mV[27]) of the SPIONs that leads to a strong electrostatic interaction with the negatively charged cell membrane surface.

After 5 h (panel H) it is possible to identify well-defined spots in the perinuclear area (similar to the

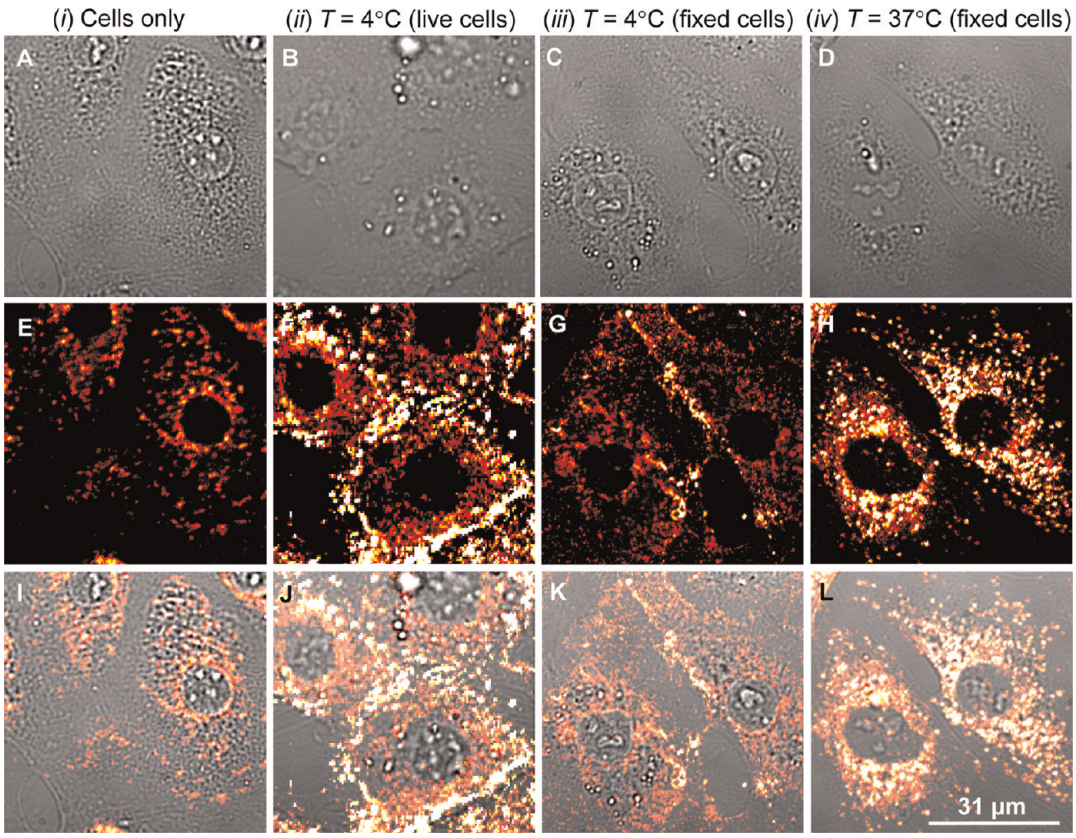

Figure 6. Bright field images (A–C), photothermal images (D–F) and overlays (G–I) for (i) cells only and cells incubated with 5 μg/mL SPIONs for 5 h at (ii) 4 °C (live cells, no rinsing of particles), (iii) 4 °C (fixed cells, rinsing of excess particles) and (iv) 37 °C (fixed cells, rinsing of excess particles).

photothermal images presented in Figure 2) indicating the accumulation of SPIONs in this region. Similar patterns in the photothermal signal were observed in all the other fields imaged at this time point. It is important to note that although the bright field images show that cells were moving and that their morphology was changing there were no significant signs of cell death.

To observe if the number of dead cells in the area scanned by photothermal microscopy was noticeably larger than in areas which had not been imaged, fluorescent images were taken at lower magnification using a 20× objective as shown in Supporting Information, Figure S9 (ii and iii). From those images, it is possible to observe that after 5.5 h cells in all areas of the dish were also stained with Sytox dyes indicating that the presence of dead cells is not particular to areas imaged by photothermal microscopy. This is also evident after 30 h, where dead cells are uniformly present in the dish. It is important to note, however, that cells proliferated in all areas of the dish leading to a confluence of approximately 90% after 30 h. Photothermal images of three different fields of live cells after a SPION labeling time of 24 h are presented in Supporting Information, Figure S10. The morphology of the cells looks good, even though each field had been scanned seven times. There is an increase in signal when compared to the images shown in Figure 5, which is presumably from the increased concentration of SPIONs within cells resulting from the long labeling period. There is also a change in distribution of the photothermal signal, with a clear change in localization from the membrane areas to the cytoplasm with maximum signal intensity in the perinuclear region.

Further insight into the nature of the cellular uptake of SPIONs has been obtained by incubating cells with 5 μg/mL SPIONs for 5 h at 4 and 37 °C as shown in Figure 6.

There is a clear change in the photothermal signal for cells incubated with particles, with the localization determined by the incubation temperature. For cells incubated with SPIONs at 4 °C, the signal is limited to the membrane regions; with almost no particles present within the cytoplasm. The imaging of the live cells incubated at 4 °C was experimentally challenging as the temperature of the microscope incubator could only be controlled above room temperature (20 °C). Temperature differences between the cell medium and the optics resulted in difficulty in maintaining focus of the lasers: indeed, rapid increase of the temperature of the medium meant endocytosis was likely to begin during either laser alignment or during the imaging. We therefore performed two experiments: one where we imaged live cells that had been incubated at 4 °C, accepting the limitations

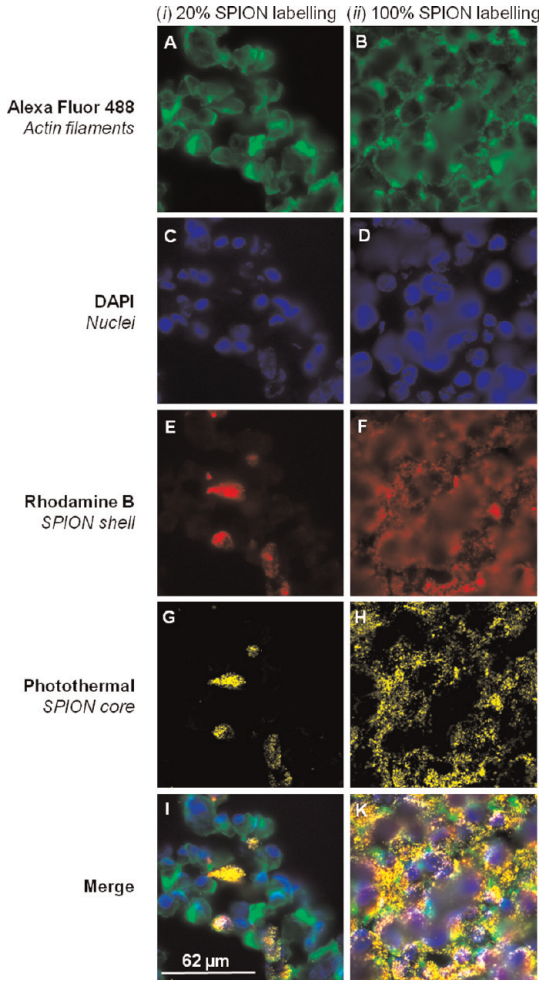

Figure 7. Images of actin filaments (green), nuclei (blue), and fluorescence from the SPION shell (red); and photothermal from the SPION core (yellow) obtained from cryosections of cell pellets containing (i) 20% cells labeled with SPIONS and (ii) 100% cells labeled with SPIONs.

mentioned above, and one where the cells were fixed at 4 °C after the initial incubation at 4 °C.

Interestingly, there is a significant difference between the 4 °C live cells and fixed cells (panels F and G), with very little SPION adsorption in membrane regions for the fixed cell sample and no significant uptake. As the fixed cell sample were rinsed several times, this suggests that no uptake occurs at 4 °C and that binding to the membrane is reversible and can be easily rinsed away. However, when cells are incubated with particles at 37 °C, there is significant uptake with a punctuate localization characteristic of endocytosis. The distribution of photothermal signal is similar to the live cell images presented in Figure 5H. This experiment confirms an energy-dependent endocytotic mechanism for the uptake of these SPIONs in kidney-derived murine stem cells. Further images taken from fixed cells after incubation with 5 μg/mL SPIONs for 5 h at 4 and 37 °C are provided in Supporting Information, Figure S11.

Having established the mechanism of particle uptake through imaging of adherent cells in a dish, we examine the possibility of identifying cells in cryosections of cell pellets. SPION-based biomedical applications require knowledge of the long-term fate of the particles *in vivo*, and in particular, the identification of SPION-labeled cells in histological sections. Such imaging is currently performed using a combination of TEM, Prussian blue staining, and fluorescence imaging; however, it is difficult to perform large systematic studies that elucidate cell-to-cell variation and allow for the identification of the presence of particles within large populations of cells.

As a proof of principle, we have prepared 7 μm thick cryosections of cell pellets and imaged using both fluorescence and photothermal microscopy. Fluorescent labeling of actin filaments and nuclei was performed in order to demonstrate the possibility of combining photothermal microscopy with standard immunofluorescence methods. Figure 7 compares fluorescence and photothermal images taken from samples where (i) 20% and (ii) 100% of the population was labeled with SPIONs, respectively. As seen previously in Figure 2, there is excellent colocalization of the fluorescence signal from the SPION shell and core, although as the fluorescence imaging is wide field there is a blurring of planes that are not in focus. In contrast, the photothermal signal yields a considerably sharper image. The very strong photothermal signal from labeled cells combined with the lack of photothermal signal from unlabeled cells shows that with this technique we can confidently distinguish between cells with and without SPION labeling.

CONCLUSIONS

We have shown the possibility to follow the uptake of SPIONs within cells by imaging the iron oxide core *via* photothermal microscopy. To our knowledge, this is the first time that this microscopy technique has been applied to image SPIONs in fixed or live cells. We have demonstrated that photothermal microscopy can accurately quantify cellular uptake using a single cell analysis approach, which is in excellent agreement with ICP-OES measurements. We have established that photothermal microscopy has a very broad dynamic range of detection, and we can identify SPIONs adsorbed on a surface, adsorbed to the cell membrane and highly localized in cellular vesicles. Finally, we have shown that we can identify cells labeled with SPIONs in cryosections where the majority of the cell population comprises unlabeled cells. This method offers two main advantages of identifying the presence of iron oxide when compared with the traditional Prussian blue staining. First, it is nondestructive and therefore suitable for *in vitro* studies. Second, it offers a higher sensitivity and resolution, thus allowing the

identification of low concentrations of SPIONs within a precise subcellular location. We suggest that this method might be of particular relevance for research involving clinically approved SPIONs, which do not contain fluorescent tags and therefore cannot be detected *via* fluorescence microscopy.

EXPERIMENTAL MATERIALS AND METHODS

SPIONs. Commercially available magnetic nanoparticles were used in this study. Molday ION Rhodamine B SPIONs (BioPAL) are superparamagnetic iron-based contrast reagents designed for cell labeling. The particles comprise an iron oxide core (of nominal diameter 8 nm), which is covered by a proprietary dextran shell cross-linked for stability. The shell is functionalized with Rhodamine B, with a nominal colloidal hydrodynamic diameter given as 35 nm (Supporting Information, Figure S1b).

Preparation of Dishes to Establish SPION Detection Threshold. Glass bottomed dishes (MatTek) were covered with 0.01% (w/v) poly(L-lysine) (Sigma) for 40 min and then rinsed three times with water. Following this, the same area was covered with 0.01% (w/v) carboxymethyldextran (Sigma) for a further 40 min and again then rinsed three times with water. The sample was then left to dry for 2 h, before adding a 5 μL drop of known 20 μg/mL SPIONs to adsorb for 30 s. Following this, the samples were rinsed three times with water and finally 4 mL of water was added before imaging *via* fluorescence and photothermal imaging.

Cell Culture. A kidney-derived murine stem cell line[37] was used as a model for cell imaging. Cells were cultured in Dulbecco's modified Eagle's medium (DMEM; Sigma) supplemented with 10% fetal bovine serum (FBS; PAA) and 2 mM L-glutamine (Sigma) under standard culture conditions (37 °C, 5% CO_2).

Preparation of Cells for Iron Quantification and Photothermal Imaging. Cells were subcultured at a density that yielded 40% confluence on the following day. The cells were then labeled with SPIONs by incubation with culture medium containing the nanoparticles at a concentration of 1, 5, or 25 μg/mL for a period of 24 h. An additional control sample where no SPION was added to the culture medium was included in every preparation. After the incubation period, cells were washed twice with phosphate buffered saline (PBS) to remove excess SPIONs from the medium, and processed accordingly for photothermal or TEM imaging. For iron quantification, the cells were grown in 6-well plates and in triplicate for each condition. After the labeling procedure, cells were trypsinized and resuspended in 1500 μL of culture medium from which a small fraction (100 μL) was taken to measure the number of cells per sample using a coulter Z2 particle analyzer. The remaining cells were centrifuged at 400*g*, the excess medium was removed, and then the cells were resuspended in 5 M hydrochloric acid for digestion. The digestion was carried out at 50 °C for 48 h, after which the amount of iron was quantified *via* ICP−OES (Spectro Ciros CCD SOP). Knowledge of the total amount of iron as well as the number of cells per sample allowed for the iron load per cell to be calculated for each condition. For photothermal imaging of fixed cells, glass bottom dishes (Greiner Bio-one) were used, and the labeled cells were fixed with 4% paraformaldehyde (PFA) for 10 min followed by three extra PBS washes to remove excess fixative. Cells were kept at 4 °C in PBS prior to imaging.

Preparation of Cells for Live Cell Imaging. Cells were seeded in glass bottom dishes containing an imprinted 50 μm relocation grid (Ibidi) and loaded onto the microscope stage for imaging. The culture medium used for live cell imaging contained no phenol red and was additionally supplemented with penicillin and streptomycin to prevent bacterial infection. Images of the unlabeled cells were acquired first, after which the cultured medium was removed and replaced with medium containing SPIONs at a concentration of 5 μg/mL in order to study uptake dynamics.

Preparation of Cell Sections. Cells labeled with SPIONs (5 μg/mL for 24 h) were trypsinised and either directly pelleted by centrifugation at 500*g* to generate pellets comprising 100% labeled cells or were mixed in a 1:5 ratio with unlabeled cells prior to centrifugation to generate pellets comprising 20% labeled cells. The pellets were fixed with 4% paraformaldehyde (PFA), transferred to a cryomold, covered with tissue embedding compound (Cryo-M-Bed, Bright Instruments Co. Ltd.), and snap frozen. Frozen sections (7 μm) were obtained with a cryostat (HM 505 N, Microm International GmbH), stained with 4′,6-diamidino-2-phenylindole (DAPI, Invitrogen) and Alexa Fluor 488 phalloidin (Invitrogen) and finally mounted with fluorescent mounting medium (Dako).

Fluorescence and Photothermal Imaging. A simplified schematic of the setup used to perform correlative microscopy of the SPION shell (*via* fluorescence) and core (*via* photothermal imaging) on a TEM grid and within cells is presented in Supporting Information, Figure S2. Imaging was performed using a customized Zeiss Axiovert 200 inverted microscope to allow for both fluorescence and photothermal imaging to be completed on the same sample. The setup used here is based upon the system developed by Lounis et al.[21−25]

Fluorescence imaging was performed in a transmission configuration using an objective (Zeiss Achroplan 40×, NA = 0.8 water dipping objective) as a condenser. The light source was an X-Cite mercury lamp (EXFO), using a Carl Zeiss excitation filter (540 nm, bandpass 25 nm) to excite the fluorophore in the ligand shell of the SPIONs. The emitted light was collected by a Zeiss Plan Apochromat 63×, NA = 1.4 oil objective lens, passed through a Carl Zeiss emission filter (605 nm, bandpass 55 nm) and captured by a Hamamatsu ImagEM CCD camera. All images were obtained using a sensitivity gain of 200 and an exposure time of 1.5 s, with the signal processed using a 4-frame rolling average.

Photothermal imaging was performed using the setup as illustrated in Supporting Information, Figure S2b. The sample was heated using a Laser Quantum ND:YAG frequency-doubled laser pump beam ($\lambda_{heating}$ = 523 nm) which was modulated at a frequency of 530.5 kHz by an acousto-optic modulator (Isomet Corporation) and set to a power of 2 mW for the SPIONs in fixed cells (1 mW for live cells). The local change in refractive index around the SPIONs was probed by a JDS Uniphase Corporation HeNe laser, (λ_{probe} = 633 nm) at a power of 9.3 mW. Both laser beams were focused to the same focal plane within the sample using a Zeiss Plan Apochromat 63×, NA = 1.4 oil objective lens. For both fixed and live cells, a Zeiss Achroplan 40×, NA = 0.8 water dipping objective was used to collect the forward interfering beam after its interaction with the sample. For cell sections, a Zeiss EC Plan-NEOFLUAR 40×, NA = 1.3 oil objective was used.

All photothermal images were acquired 1 μm above the top surface of the glass bottom dish. The area of interest (in this case 256 × 256 pixels) was raster scanned by moving a piezo-electric device (Physik Instrument) over the fixed laser beams, with the collected light focused onto a photodiode. For each pixel, the magnitude of the probe beam forward interfering field at 530.5 kHz was extracted using a lock-in amplifier and digitized, with the image constructed by integrating the signal in each pixel over a time of 10 ms. Imaging was performed at one of two resolutions with the effective pixel size either 244 or 488 nm, respectively.

Prussian Blue Staining. Following photothermal imaging of fixed cells, the buffer was removed and the Prussian blue reagent (Iron Stain Kit; Sigma) was added and left to develop for 20 min. The image was captured using a ThorLabs DC 310-C color CCD camera. The bright field illumination was performed using the top objective as a condenser and not dipping in the solution as the acid would damage the lens.

Conflict of Interest: The authors declare no competing financial interest.

Acknowledgment. The authors would like to thank I. Prior for the use of his electron microscopy facilities in the Physiology Laboratory, University of Liverpool. This work was supported by EPSRC Grant EP/H046143/1 and was also partially funded by the Marie Curie EU Grant PERG08-GA-2010-276909.

Supporting Information Available: Details of the SPIONs absorbance properties, experimental set up for fluorescence and photothermal imaging, calculations establishing the detection sensitivity of the photothermal, TEM imaging of SPIONs in cells, single cell analysis of photothermal imaging, image analysis of Prussian blue images, cytotoxicity assays, and live cell imaging. This material is available free of charge *via* the Internet at http://pubs.acs.org.

REFERENCES AND NOTES

1. Pankhurst, Q. A.; Connolly, J.; Jones, S. K.; Dobson, J. Applications of Magnetic Nanoparticles in Biomedicine. *J. Phys. D* **2003**, *36*, R167–181.
2. Pankhurst, Q. A.; Thanh, N. K. T.; Jones, S. K.; Dobson, J. Progress in Applications of Magnetic Nanoparticles in Biomedicine. *J. Phys. D* **2009**, *42*, 224001.
3. Gupta, A. K.; Gupta, M. Synthesis and Surface Engineering of Iron Oxide Nanoparticles for Biomedical Applications. *Biomaterials* **2005**, *26*, 3995–4021.
4. Laurent, S.; Forge, D.; Port, M.; Roch, A.; Robic, C.; Elst, L. V.; Muller, R. N. Magnetic Iron Oxide Nanoparticles: Synthesis, Stabilisation, Vectorisation, Physicochemical Characterisations, and Biological Applications. *Chem. Rev.* **2008**, *108*, 2064–2110.
5. Neuberger, T.; Schopf, B.; Hofmann, H.; Hofmann, M.; von Rechenberg, B. Superparamagnetic Nanoparticles for Biomedical Applications: Possibilities and Limitations of a New Drug Delivery System. *J. Magn. Magn. Mater.* **2005**, *293*, 483–496.
6. Taylor, A.; Wilson, K. M.; Murray, P.; Fernig, D. G.; Lévy, R. Long-Term Tracking of Cells Using Inorganic Nanoparticles as Contrast Agents: Are We There Yet?. *Chem. Soc. Rev.* **2012**, *41*, 2707–2717.
7. Xu, C.; Mu, L.; Roes, I.; Miranda-Nieves, D.; Nahrendorf, M.; Ankrum, J. A.; Zhao, W.; Karp, J. M. Nanoparticle-Based Monitoring of Cell Therapy. *Nanotechnology* **2011**, *22*, 494001.
8. Levy, M.; Luciani, N.; Alloyeau, D.; Elgrabi, D.; Deveaux, V.; Pechoux, C.; Wang, G.; Vats, N.; Gendron, F.; Factor, C.; *et al.* Long Term *in Vivo* Biotransformation of Iron Oxide Nanoparticles. *Biomaterials* **2011**, *32*, 3988–3999.
9. Arbab, A. S.; Wilson, L. B.; Ashari, P.; Jordan, E. K.; Lewis, B. K.; Frank, J. A. A. Model of Lysosomal Metabolism of Dextran Coated Superparamagnetic Iron Oxide (SPIO) Nanoparticles: Implications for Cellular Magnetic Resonance Imaging. *NMR Biomed.* **2005**, *18*, 383–389.
10. Skotland, T.; Sontum, P. C.; Oulie, I. In *Vitro* Stability Analyses as a Model for Metabolism of Ferromagnetic Particles (Clariscan((TM))), a Contrast Agent for Magnetic Resonance Imaging. *J. Pharmaceut. Biomed. Anal.* **2002**, *28*, 323–329.
11. Soenen, S. J. H.; Himmelreich, U.; Nuytten, N.; Pisanic, T. R.; Ferrari, A.; De Cuyper, M. Intracellular Nanoparticle Coating Stability Determines Nanoparticle Diagnostics Efficacy and Cell Functionality. *Small* **2010**, *6*, 2136–2145.
12. Bogart, L. K. An Investigation of the Structure, Pinning and Magnetoresistance of Domain Walls in $Ni_{81}Fe_{19}$ Planar Nanowires, Ph.D. Thesis, Durham University, Durham, England, 2010.
13. Jendelova, P.; Herynek, V.; Urdzíková, L.; Glogarová, K.; Kroupová, J.; Andersson, B.; Bryja, V.; Burian, M.; Hájek, M.; Syková, E. Magnetic Resonance Tracking of Transplanted Bone Marrow and Embryonic Stem Cells Labelled by Iron Oxide Nanoparticles in Rat Brain and Spinal Cord. *J. Neurosci. Res.* **2004**, *76*, 232–243.
14. Zhou, T.; Wu, B.; Xing, D. Bio-modified Fe_3O_4 core/Au shell nanoparticles for targeting and multimodal imaging of cancer cells. *J. Mater. Chem.* **2012**, *22*, 470–477.
15. Mohammad, F.; Balajim, G.; Weber, A; Uppu, R. M.; Kumar, C. S. S. R. Influence of Gold Nanoshell on Hyperthermia of Superparamagnetic Iron Oxide Nanoparticles. *J. Phys. Chem. C* **2010**, *114*, 19194–19201.
16. Hormes, J.; Modrow, H.; Bonnemann, H.; Kumar, C. J. The Influence of Various Coatings on the Electronic, Magnetic, and Geometric Properties of Cobalt Applications. *Appl. Phys. Lett.* **2005**, *97*, 10R102–10R106.
17. Schulze, E.; Ferrucci, J. T.; Poss, K.; Lapointe, L.; Bogdanova, A.; Weissleder, R. Cellular Uptake and Trafficking of a Prototypical Magnetic Iron Oxide Label in *Vitro*. *Invest. Radiol.* **1995**, *30*, 604–610.
18. Moore, A.; Weissleder, R.; Bogdanov, A., Jr Uptake of Dextran-Coated Monocrystalline Iron Oxides in Tumor Cells and Macrophages. *J. Magn. Reson.* **1997**, *7*, 1140–1145.
19. Sée, V.; Free, P.; Cesbron, Y.; Nativo, P.; Shaheen, U.; Rigden, D. J.; Spiller, D. G.; Fernig, D. G.; White, M. R. H.; Prior, I. A.; *et al.* Cathespin L Digestion of Nanobioconjugates Upon Endocytosis. *ACS Nano* **2009**, *3*, 2461–2468.
20. Berciaud, S.; Lasne, D.; Blab, G. A.; Cognet, L.; Lounis, B. Photothermal Heterodyne Imaging of Individual Metallic Nanoparticles: Theory *versus* Experiment. *Phys. Rev. B* **2006**, *73*, 045424.
21. Berciaud, S.; Cognet, L.; Tamarat, P.; Lounis, B. Observation of Intrinsic Size Effects in the Optical Response of Individual Gold Nanoparticles. *Nano Lett.* **2005**, *5*, 515–518.
22. Lasne, D.; Blab, G. A.; Berciaud, S.; Heine, M.; Groc, L.; Choquet, D.; Cognet, L.; Lounis, B. Single Nanoparticle Photothermal Tracking (SNaPT) of 5-nm Gold Beads in Live Cells. *Biophys. J.* **2006**, *91*, 4598–4604.
23. Berciaud, S.; Cognet, L.; Blab, G. A.; Lounis, B. Photothermal Heterodyne Imaging of Individual Non-fluoresent Nanoclusters and Nanocrystals. *Phys. Rev. Lett.* **2004**, *93*, 257402.
24. Berciaud, S.; Cognet, L.; Poulin, P.; Weisman, R. B.; Lounis, B. Absorption Spectroscopy of Individual Single-Walled Carbon Nanotubes. *Nano Lett.* **2007**, *7*, 1203–1207.
25. Berciaud, S.; Cognet, L.; Lounis, B. Luminescence Decay and the Absorption Cross Section of Individual Single-Walled Carbon Nanotubes. *Phys. Rev. Lett.* **2008**, *101*, 077402.
26. Kim, J.; Oh, J.; Kang, H. W.; Feldman, M. D.; Milner, T. E. Photothermal Response of Superparamagnetic Iron Oxide Nanoparticles. *Laser. Surg. Med.* **2008**, *40*, 415–421.
27. BioPal (Biophysics Assay Laboratories), Molday Ion Catalogue (Iron oxide-based superparamagnetic contrast agents); http://www.biopal.com/images/Molday%20ION.pdf (accessed 1st February 2012).
28. Sun, S.; Murray, C. B.; Weller, D.; Folks, L.; Moser, A. Monodisperse FePt Nanoparticles and Ferromagnetic FePt Nanocrystal Superlattices. *Science* **2000**, *287*, 1989–1992.
29. Klahr, B. M.; Martinson, A. B. F.; Hamann, T. W. Photoelectrochemical Investigation of Ultrathin Film Iron Oxide Solar Cells Prepared by Atomic Layer Deposition. *Langmuir* **2011**, *27*, 461–468.
30. Cherepy, N. J.; Liston, D. B.; Lovejoy, J. A.; Deng, H. M.; Zhang, J. Z. Ultrafast Studies of Photoexcited Electron Dynamics in Gamma- and Alpha-Fe_2O_3 Semiconductor Nanoparticles. *J. Phys. Chem. B* **1998**, *102*, 770–776.
31. Cornell, R. M., Schwertmann, U. *The Iron Oxides*; VCH: New York, 1996.
32. He, Y. P.; Miao, Y. M.; Li, C. R.; Wang, S. Q.; Cao, L; Xie, S. S.; Yang, G. Z.; Zou, B. S.; Burda, C. Size and Structure Effect on Optical Transitions of Iron Oxide Nanocrystals. *Phys. Rev. B* **2005**, *71*, 125411.
33. Lindgren, T.; Wang, H. L.; Beermann, N.; Vayssieres, L.; Hagfeldt, A.; Lindquist, S. E. Aqueous Photoelectrochemistry of Haematite Nanorod Array. *Sol. Energy Mater. Sol. C.* **2002**, *71*, 231–243.

34. Bjorksten, U.; Moser, J.; Gratzel, M. Photoelectrochemical Studies on Nanocrystalline Haematite films. *Chem. Mater.* **1994**, *6*, 858–863.
35. This assumes that all SPIONs in the droplet have adsorbed on the polymer surface.
36. Lasne, D.; Blab, G. A.; De Giorgi, F.; Ichas, F.; Lounis, B.; Cognet, L. Label-free Optical Imaging of Mitochondria in Live Cells. *Opt. Express.* **2007**, *15*, 14184–14193.
37. Fuente Mora, C.; Ranghini, E.; Bruno, B.; Bussolati, B.; Camussi, G.; Wilm, B.; Edgar, D.; Kenny, S.; Murray, P. Differentiation of podocyte and proximal tubule-like cells from a mouse kidney-derived stem cell line. *Stem Cells Dev.* **2012**, *21*, 296–307.